

FULL PAPER

Open Access



# Spatial–temporal properties of afterslip associated with the 2015 Mw 8.3 Illapel earthquake, Chile

Yunfei Xiang<sup>1\*</sup>, Jianping Yue<sup>2</sup>, Zhongshan Jiang<sup>3</sup> and Yin Xing<sup>2</sup>

## Abstract

In order to characterize the spatial–temporal properties of postseismic slip motions associated with the 2015 Illapel earthquake, the daily position time series of 13 GNSS sites situated at the near-field region are utilized. Firstly, a scheme of postseismic signal extraction and modeling is introduced, which can effectively extract the postseismic signal with consideration of background tectonic movement. Based on the extracted postseismic signal, the spatial–temporal distribution of afterslip is inverted under the layered medium model. Compared with coseismic slip distribution, the afterslip is extended to both deep and two sides, and two peak slip patches are formed on the north and south sides. The afterslip is mainly cumulated at the depth of 10–50 km, and the maximum slip reaches 1.46 m, which is situated at latitude of  $-30.50^\circ$ , longitude of  $-71.78^\circ$ , and depth of 18.94 m. Moreover, the postseismic slip during the time period of 0–30 days after this earthquake is the largest, and the maximum of fault slip and corresponding slip rate reaches 0.62 m and 20.6 mm/day. Whereas, the maximum of fault slip rate during the time period of 180–365 days is only around 1 mm/day. The spatial–temporal evolution of postseismic slip motions suggests that large postseismic slip mainly occurs in the early stage after this earthquake, and the fault tend to be stable as time goes on. Meanwhile, the Coulomb stress change demonstrate that the postseismic slip motions after the Illapel earthquake may be triggered by the stress increase in the deep region induced by coseismic rupture.

**Keywords:** GNSS position time series, Postseismic signal, Afterslip, Postseismic slip motions, Spatial–temporal properties

## Introduction

In general, the postseismic deformations with logarithmic or exponential decay can be observed after many large tectonic earthquakes due to the fault instability and coseismic stress transfer. Numerous studies indicate that the main factors of postseismic deformations contain afterslip, viscoelastic relaxation, and poroelastic rebound (Segall and Davis 1997; Hsu et al. 2002, 2006; Politz et al. 2006; Freed 2007; Bruhat et al. 2011; Hoecher et al. 2012). Among them, the effects of afterslip and viscoelastic relaxation are relatively significant in comparison with

poroelastic rebound. Meanwhile, the effects of afterslip are cumulated at the near-field region of the source in the early stage after the earthquake occurrence, while the effects of viscoelastic relaxation are cumulated at the middle- and far-field regions in the long-term period. Characterizing the properties of postseismic slip is helpful for understanding the stability of fault and the rheological properties of earth's medium, which is of great significance for the postseismic disaster risk assessment (Kreemer et al. 2006; Diao et al. 2011, 2018; Ozawa et al. 2012; Jiang et al. 2017, 2018). Compared with other space geodesy technology, GNSS technology has high positioning accuracy (the accuracy of daily solution can reach millimeters) and high time resolution (Shen et al. 2009; Guo et al. 2012; Simons et al. 2011; Diao et al. 2012). Therefore, GNSS has incomparable advantages

\*Correspondence: yfxiang181@163.com

<sup>1</sup> College of Civil Engineering, Nanjing Forestry University, Nanjing 210037, China

Full list of author information is available at the end of the article

for exploring the postseismic deformations during the period of months, 1 year, or several years. The continuous GNSS network can accurately detect the postseismic signal, which can provide valuable data sets for exploring the spatial–temporal properties of afterslip after some large earthquakes.

According to United States Geological Survey (USGS), a Mw 8.3 earthquake struck the coastal area of central Chile on 16 September 2015. Numerous studies associated with coseismic and postseismic deformations of this earthquake have been carried out. Chen et al. (2016) utilized GPS/GLONASS to determine the real-time coseismic displacements of the Mw 8.3 Illapel earthquake, and revealed that GPS/GLONASS provided more accurate and robust coseismic displacements in comparison with GPS-only. Meanwhile, the coseismic slip distributions of the Illapel earthquake determined by the GPS/GLONASS observations tended to be shallower and larger. Okuwaki et al. (2016) proposed a seismic source of the Illapel earthquake, and characterized the rupture process with a novel kinematic waveform inversion method. The spatiotemporal properties of coseismic slip revealed a complex rupture propagation mode: two up-dip rupture propagation events, and the second rupture event may be triggered by strong high-frequency radiation events. Heidarzadeh et al. (2016) reconstructed the source model of the Illapel earthquake using teleseismic and tsunami data, and tried to explore the relationship between 2010 Maule and 2015 Illapel earthquakes. Williamson et al. (2017) characterized the coseismic slip model of this earthquake by the combined use of GPS, InSAR, and tsunami waveform data. The coseismic slip showed that most coseismic slip was cumulated at a region immediately offshore, and there was almost no obvious slip near the trench. Melgar et al. (2016) adopted geodetic observations to resolve a kinematic slip model, and found the shallow and deep sections of the megathrust were segmented and had fundamentally different behavior. Ruiz et al. (2016) estimated the coseismic rupture process of the Illapel earthquake based on teleseismic P-waves and strong-motion records, and revealed most of aftershocks focused on the deeper section of the plate interface. Barnhart et al. (2016) characterized the coseismic slip and early afterslip of the Illapel earthquake using GPS and InSAR observations. The result indicated that early afterslip after this earthquake appeared in two regions around the coseismic slip with partial overlap. Huang et al. (2017) explored the spatiotemporal properties of early afterslip and aftershocks using the postseismic GPS and InSAR data. The spatial distribution of aftershocks was consistent with that of afterslip inverted by geodetic observations, which seemed to surround the coseismic slip.

The above studies associated with the 2015 Illapel earthquake have revealed the coseismic slip, coseismic rupture process, early afterslip, and aftershocks based on

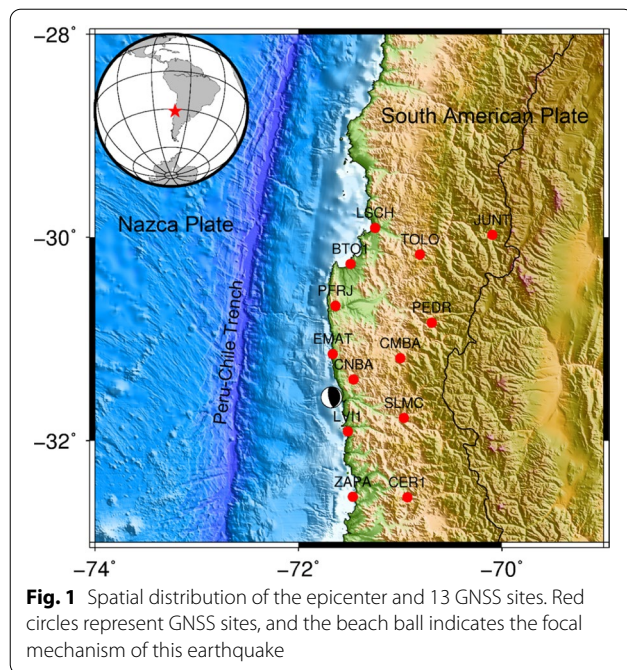
multi-source observations. However, few studies focus on exploring the spatial–temporal properties of afterslip after this earthquake, as well as the Coulomb stress change. Characterizing the spatial–temporal properties of postseismic slip behavior is of great significance to the assessment of the fault stability and postseismic disaster risk. In addition, considering the influence of the Mw 7.3 aftershock on 25 December 2016, the time span of GNSS position time series after this earthquake is selected to be 1 year. Thus, the GNSS observations of 13 sites during the 1 year after this earthquake are utilized to explore the spatial–temporal properties of postseismic fault slip behavior in this paper. Meanwhile, we also discuss the Coulomb stress change after this earthquake, which will be helpful for understanding the triggering mechanism of postseismic slip motions.

## Data sets and methods

### Regional tectonic background and GNSS data

The 2015 Illapel earthquake occurs at the region where the Nazca plate collides with the South American plate, which is the seismic active area in Chile (Shrivastava et al. 2016; Barnhart et al. 2016). The epicenter is located at the latitude and longitude of 31.57°S and 71.67°W, and the focal depth is 22.4 km. The Nazca plate subducts to the South American plate at a speed of approximately 74 mm/year along the northeast, and collides beneath the Peru–Chile Trench. Meanwhile, the rupture zone of this earthquake is laterally constrained by two prominent structural features: the Challenger fault zone (CFZ) in the north and the Juan Fernandez ridge (JFR) in the south. Historically, many large thrust-type earthquakes occur in the region, including the 1960 M 9.5 earthquake, the 2010 Mw 8.8 earthquake, and several M 7 + earthquakes.

In order to characterize the postseismic deformation mechanism and spatial–temporal properties of afterslip, the daily position time series of 13 GNSS sites situated at the near-field region are utilized (Fig. 1). In general, the postseismic GNSS position time series also contains plate tectonic movement signal. Thus, the GNSS observations of 13 sites with time span of about 2 years before the earthquake are chosen to estimate the plate tectonic signal. The GNSS position time series of 13 sites are provided by Nevada Geodetic Laboratory (NGL), which are available at <http://geodesy.unr.edu/>. The data processing is conducted by GIPSY-OASIS-II. NGL data processing center utilizes ionospheric independent combination to remove ionospheric effects, Global Mapping Function (GMF) model to correct tropospheric delays, FES 2004 to correct tidal loading effects, and antenna phase center correction parameters refer to the absolute antenna phase calibration file provided by IGS center.



### Postseismic signal extraction scheme

In general, the postseismic GNSS position time series mainly contains long-term trend signal caused by plate tectonic movement, seasonal signal induced by surface mass loading (i.e., atmospheric pressure, non-tidal oceanic change, and hydrological loading), postseismic signal, and noise (e.g., white and colored noise) (Zhou et al. 2020). Among them, the postseismic signal can usually be expressed in logarithmic or exponential form. In order to extract the postseismic signal, we should model and remove the effects of other signals. The preseismic GNSS position time series with time span of about 2 years is utilized to estimate the long-term plate movement rate. Based on the above discussion, we design a scheme for extracting and modeling postseismic signal with considering the influence of plate tectonic motions, surface mass loading, and clear noise. The scheme of postseismic signal extraction mainly contains the following steps:

#### (1) Outlier detection and elimination

Due to the influence of abnormal observation environment and other factors, there are usually a small number of outliers in the GNSS observations, which greatly deviate from normal observations. For outlier detection and elimination, we first roughly eliminate the GNSS

observations with errors > 20, 20, and 40 mm in the north, east, and up components. After that, the outliers in the GNSS position time series are detected and eliminated by the combined use of inter-quartile range (IQR) and  $3\sigma$  rules.

#### (2) Velocity interpolation

Due to the influence of background tectonic movement, the horizontal components of GNSS position time series generally have significant linear trend term, which can reach several centimeters per year. Therefore, the linear trend term in GNSS position time series caused by background tectonic movement should be considered for the postseismic signal extraction. Whereas, some key sites used to study the postseismic deformations may have missed preseismic GNSS observations. Considering this problem, this paper mainly utilizes the velocity interpolation to estimate the linear trend term caused by the background tectonic movement for these sites, and the spatial interpolation is utilized to estimate the three-dimensional crustal movement rate based on the GNSS velocity field around these sites. For the velocity interpolation, the velocity interpolation for strain rate (VISR) program developed by Shen et al. (2015) is adopted.

#### (3) Determination of relax time constant

Before parameter estimation, the relaxation time constant must be determined and the non-linear function model should be converted into a linear model, and then the parameter estimation can be accomplished. For the determination of relaxation time constant, the Nelder–Mead simplex method is firstly utilized to roughly estimate the relaxation time constant of each site by means of seeking a local optimal solution. According to the roughly estimated relaxation time constant, the approximate range of relaxation time constant is determined. Then, the trial and error method is utilized to search for the optimal relaxation time constant.

#### (4) Parameter estimation

Considering the influence of background tectonic movement, it is not reasonable to adopt only logarithmic or exponential function to simulate postseismic deformations (Tobita 2016). When the preseismic GNSS observations are added, the entire position time series can be expressed by the following formula:

$$\begin{aligned}
 y(t) = & y_0 + vt + A \sin(2\pi t) + B \cos(2\pi t) + C \sin(4\pi t) \\
 & + D \cos(4\pi t) + \sum_{j=1}^k O_j H(t - t_{0j}) \\
 & + \sum_{l=1}^m H(t - tq_l) \left( c_l + p_l \ln \left( 1 + \frac{t - tq_l}{\tau_l^{\log}} \right) \right) \\
 & + b_l \left( 1 - \exp \left( -\frac{t - tq_l}{\tau_l^{\exp}} \right) \right) + \Delta v_l \pi + \varepsilon.
 \end{aligned} \tag{1}$$

Among them,  $t$  is the epoch time in years,  $y_0$  is the initial position of GNSS site,  $vt$  is the linear trend term caused by background plate tectonic movement,  $A \sin(2\pi t) + B \cos(2\pi t) + C \sin(4\pi t) + D \cos(4\pi t)$  is the seasonal term induced by surface mass loading,  $\sum_{j=1}^k O_j H(t - t_{0j})$  is the offsets caused by non-seismic factors,  $\sum_{l=1}^m c_l H(t - tq_l)$  is coseismic offsets,  $\sum_{l=1}^m p_l \ln \left( 1 + \frac{t - tq_l}{\tau_l^{\log}} \right) + b_l \left( 1 - \exp \left( -\frac{t - tq_l}{\tau_l^{\exp}} \right) \right)$  is the postseismic signal expressed as logarithmic or exponential form,  $\Delta v_l$  is the crustal movement rate altered by earthquake, and  $\varepsilon$  is the systemic errors. For parameter estimation of GNSS position time series, least square parameter estimation is a general and robust method. However, the noise properties of GNSS position time series may have changed due to the influence of earthquake. Thus, maximum likelihood estimation (MLE) is utilized to simultaneously estimate the parameters and noise of GNSS position time series, and then extract and model the postseismic signal.

### Fault slip inversion method

The dislocation theory is the theoretical basis of fault slip inversion, and Okada elastic dislocation model establishes the elastic response relationship between fault dislocation and crustal deformation. The function model can be expressed as:

$$y = f(x) + \varepsilon, \tag{2}$$

where  $x$  represents parameters related to fault (e.g., strike, dip, rake, length, and width), and  $\varepsilon$  denotes the errors. It can be seen from the above formula that the crustal deformation can be regarded as the function of earth model parameter, fault geometric parameter, and dislocation parameter. After determining the fault geometric parameter, the inversion problem of dislocation model can be transformed into linear inversion, which can be expressed as:

$$y = Gs + \varepsilon, \tag{3}$$

where  $G$  is the green function, which denotes the elastic response of surface deformation to the unit fault slip,  $s$

denotes the fault slip, and  $y$  denotes the surface deformation. The calculation of green function involves the selection of earth model, which can be divided into uniform half-infinite space dislocation model, layered half-infinite space dislocation model, spherical uniform dislocation model, and spherical layered dislocation model.

Okada elastic dislocation theory establishes the spatial response of surface deformation to fault dislocation under the uniform semi-infinite space dislocation model. This method has fast calculation speed and high accuracy, and is widely used in seismic research field. However, due to the inhomogeneity of earth medium, the inversion of fault slip under the uniform semi-infinite space dislocation model maybe not reliable. Wang et al. (2013) extended the theory to the layered half-infinite space dislocation model based on Okada elastic dislocation theory, and proposed the steepest descent method (SDM) for the inversion of fault slip under layered medium model. Thus, the inversion of fault slip can be expressed as:

$$f(s) = \|y - Ms\|^2 + \beta^2 \|Hs\|, \tag{4}$$

$$\|Hs\| = \left\| \frac{\partial^2}{\partial x^2} \tau(s) + \frac{\partial^2}{\partial y^2} \tau(s) \right\|^2, \tag{5}$$

where  $s$  is the fault slip,  $y$  is the surface deformation,  $M$  is the Green function,  $\tau(s)$  is the stress drop, and  $\beta$  is the smoothing factor.  $\|y - Ms\|^2$  indicates the data misfit, and  $\beta^2 \|Hs\|$  indicates the model roughness. In general, it is suitable to utilize the trade-off value of data misfit and model roughness as the smoothing factor. In order to improve the efficiency and accuracy of fault slip inversion, the inversion process can be strongly constrained by setting relevant parameters:

$$|s_i| < s_{\max}, \varphi_{\min} \leq \varphi_i \leq \varphi_{\max}, \tag{6}$$

where  $s_i$  and  $\varphi_i$  are the slip and rake of sub-fault  $i$ .  $s_{\max}$ ,  $\varphi_{\min}$ , and  $\varphi_{\max}$  denote the maximum slip, minimum and maximum rake, respectively.

## Results and discussion

### Postseismic signal extraction

After the 2015 Illapel earthquake, the GNSS position time series of 13 sites located near the epicenter occur significant logarithmic signals. In order to characterize the spatial-temporal properties of afterslip, the scheme of signal extraction and modeling described in Sect. 2.2 is utilized to extract the postseismic signal. Taking the site CMBA as an example, this scheme is utilized to extract the postseismic signal. The time span of the GNSS position time series of site CMBA is 2013.0021–2015.7070,

and there are two offsets caused by non-seismic factors. The postseismic signal of site CMBA in three components is attenuated in logarithmic form, and some studies have revealed that the short-term near-field postseismic deformation is mainly caused by the afterslip. Thus, the logarithmic function model is adopted to simulate the postseismic deformations. Firstly, the successive iterative processing of IQR and  $3\sigma$  is performed until all the outliers in the GNSS position time series are removed. Then, the optimal relaxation time constant of this site can be identified as 8 days by the combined use of the Nelder–Mead simplex method and trial and error method. Finally, MLE is utilized to estimate the parameters of GNSS position time series, and then extract and model the postseismic signal. Figure 2 describes the GNSS position time series of site CMBA and modeled signal. The linear rates caused by crustal tectonic movement in the GNSS position time series of site CMBA in the north, east, and up components are 22.17, 21.17, and 6.83 mm/year, respectively. The weighted root mean square errors of the position time series in the north, east, and up are 2.038, 2.848, and 5.495 mm, respectively. In total, there are 3 offsets in the entire position time series. Among them, 2 offsets caused by non-seismic factors are 2014.0014 and 2014.2752, and the values of 2 offsets in

the up component reach  $-36.27$  and  $31.24$  mm, respectively. Meanwhile, the coseismic offsets in the north, east, and up components are 3.8,  $-879.2$ , and  $-131.6$  mm, respectively. Figure 3 depicts the GNSS position time series after removing the linear trend caused by plate tectonic movement and repairing 3 offsets.

Figure 4 shows the postseismic GNSS position time series and modeled postseismic signal. It can be seen that the postseismic signal attenuated in logarithmic form appears in 3 directions of site CMBA. Among them, the attenuation amplitude of postseismic signal in the east component is the largest, reaching  $-35.50$  mm, followed by the up component, and the attenuation amplitude of model signal is  $-16.30$  mm. Compared with the east and up components, the attenuation amplitude of modeled signal in the north component is the smallest (only  $-0.98$  mm). According to the attenuation amplitude, relaxation time constant, and function model, the cumulative postseismic deformations of site CMBA during the 1 year after this earthquake can be determined, and the postseismic deformations in the north, east, and up components are  $-3.59$ ,  $-132.36$ , and  $-60.96$  mm, respectively. After removing seasonal and postseismic signal, the residual GNSS position time series are depicted as Fig. 5, which mainly contains residual terms,

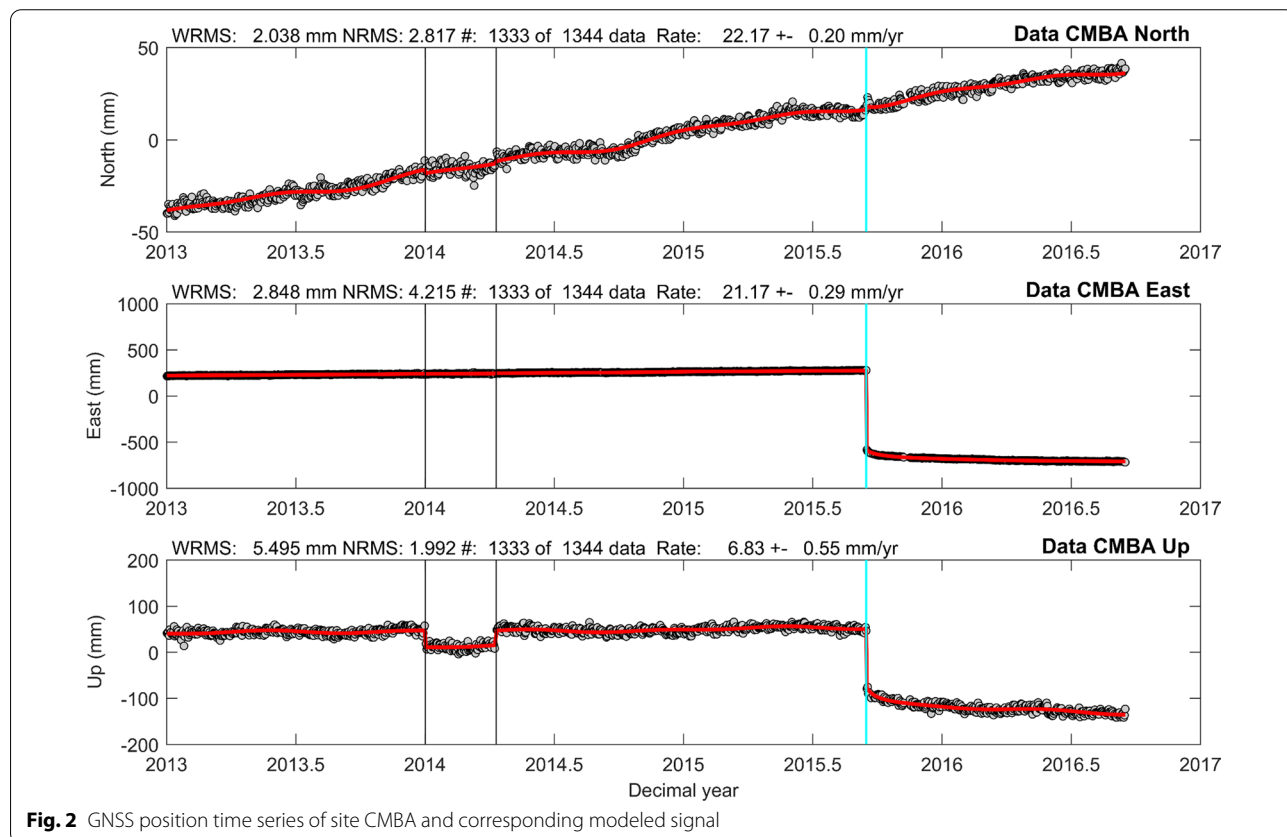


**Fig. 2** GNSS position time series of site CMBA and corresponding modeled signal

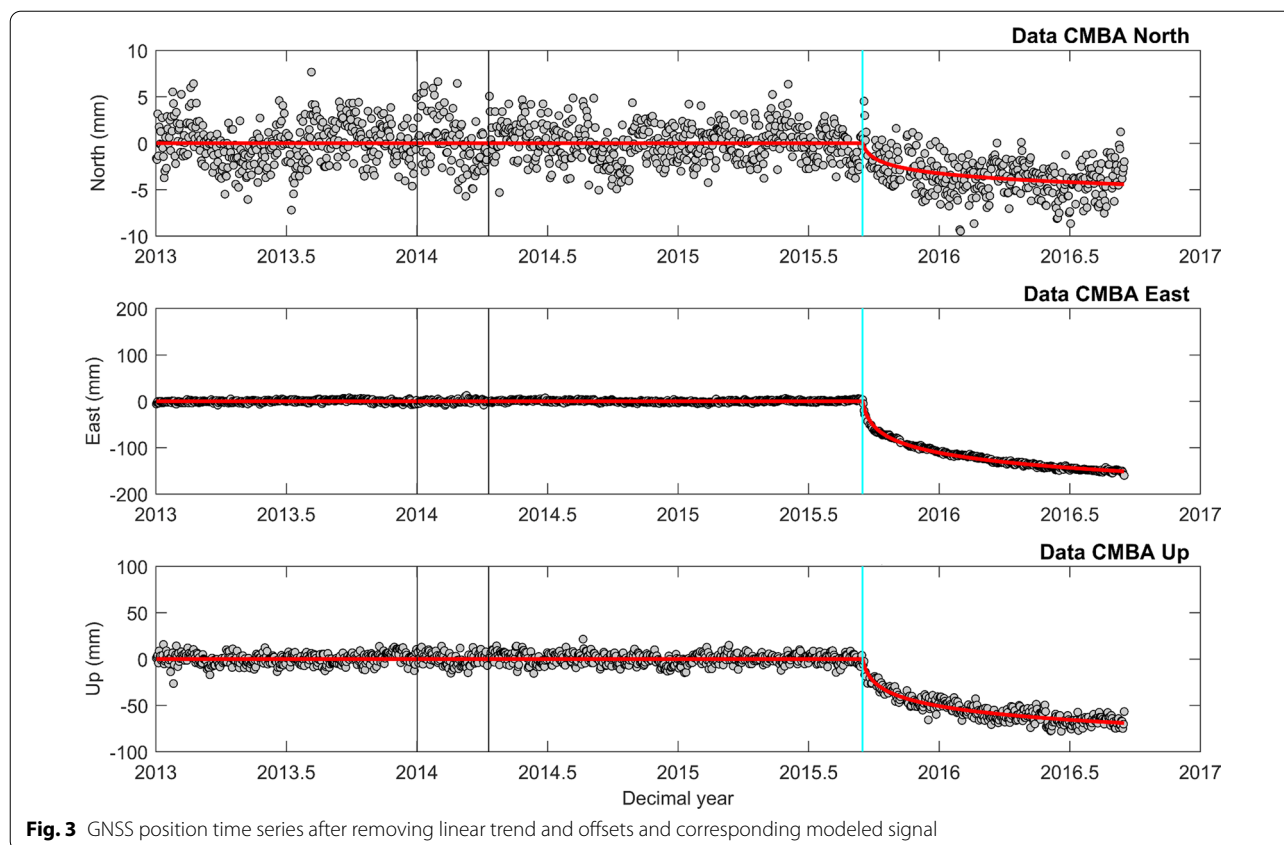


**Fig. 3** GNSS position time series after removing linear trend and offsets and corresponding modeled signal

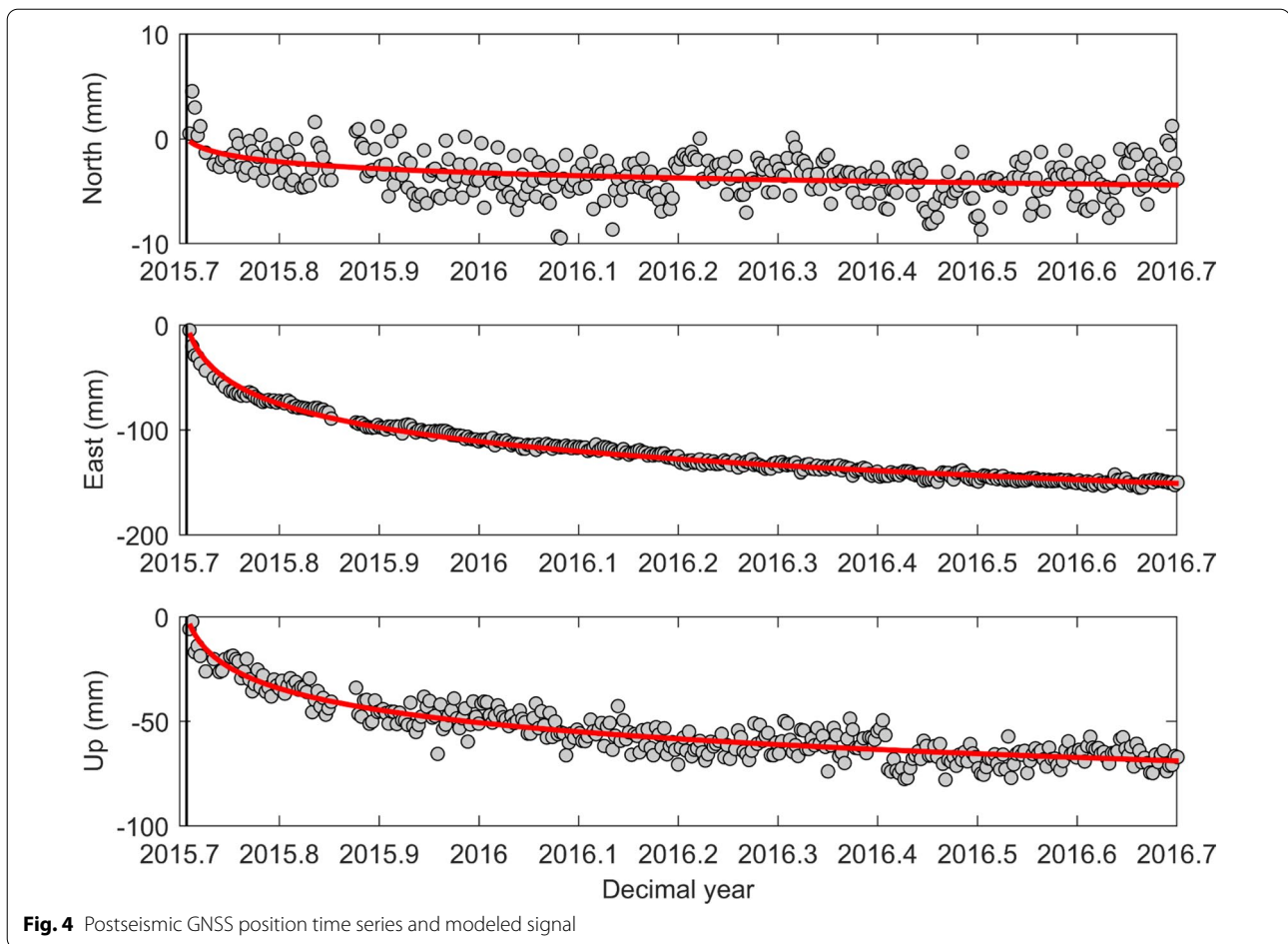
white noise, and colored noise. There is no obvious difference in morphological change between the preseismic and postseismic residual time series, and there is no periodic fluctuation, indicating that the tectonic signals, non-tectonic signals, offsets, and postseismic signal have been effectively removed.

Based on this method, the postseismic signal of other GNSS sites are extracted, and Fig. 6 shows the extracted postseismic signal of sites CNBA, PEDR, LVII, and LSCH. It can be seen that the postseismic signal in the GNSS position time series of site PEDR is similar to site CMBA. This phenomenon may be due to that the 2 sites are relatively close to each other and have a similar response to postseismic deformation mechanism. For the 4 sites, the most obvious attenuation signals appear in the east component and the attenuation amplitudes are the largest. The cumulative deformations of the 4 sites during the 1 year after this earthquake reach  $-81.57$ ,  $-153.72$ ,  $-132.39$  and  $-136.13$  mm. Secondly, it is the up component, and the cumulative deformations are  $-53.19$ ,  $-49.91$ ,  $-32.66$ , and  $-31.91$  mm, respectively. Table 1 presents the coseismic offsets of the 13 GNSS sites and the cumulative deformations during the 1 year after this earthquake. The above results indicate that the postseismic signal extraction and modeling scheme introduced in

this paper can effectively extract postseismic signal and estimate parameters of GNSS position time series with consideration of the influence of background tectonic movement. Meanwhile, this scheme performs parameter estimation of GNSS position time series through the overall modeling, which can effectively reduce the error introduced by the segmented processing.

### Coseismic slip inversion

In order to characterize the postseismic fault slip, we should firstly determine the distribution of coseismic fault slip, which can be regarded as a reference to understand the spatial-temporal properties of postseismic slip. USGS conducts the preliminary inversion of coseismic slip using the teleseismic broadband waveform, and confirms that the nodal plane with the strike and dip of  $6^\circ$  and  $19^\circ$  fits well with waveform data. According to the relevant information provided by USGS, we construct a fault model with the length and width of 288 and 160 km along the strike and dip. The fault is divided into  $10 \times 10$  km sub-faults, and the number of sub-faults is 464. Based on the theory of elastic dislocation, SDM is utilized to determine the coseismic slip under the layered medium model. The Green function of dislocation is generated by DGRN code developed by Wang et al. (2003),



and the earth model parameters adopt the model parameters provided by USGS.

Hreinsdottir et al. (2006) and Ding et al. (2015) confirmed that it is reasonable to use the difference of the average value of 4 daily coordinates of GNSS site before and after the earthquake to estimate the offset, which can effectively reduce the noise in GNSS observations and the effect of postseismic deformations. Based on this method, the offsets of 13 GNSS sites are calculated, and the coseismic deformations field is depicted as Fig. 7. It can be seen that large coseismic deformations are mainly cumulated at the near-field region of the epicenter, and the coseismic deformations decreases with the epicentral distance increasing. For the horizontal components, the largest coseismic deformation occurs at site EMAT, reaching  $-2.1681$  m in the east component. The ranges of coseismic deformations of 13 GNSS sites in the east and north component are  $-2.1681$  to  $-0.0480$  and  $-0.2333$  to  $0.1273$  m, respectively. For the vertical component, the coseismic deformations vary from  $-0.2503$  and  $0.2084$  m, and it reaches  $-0.2503$  m at site PFRJ.

According to the fault model and coseismic deformations, the coseismic slip can be characterized under the layered medium model. In order to retrieve the smooth and accurate fault slip model, the trade-off value of data misfit and model roughness is regarded as the optimal smoothing factor. Considering the weight of data misfit and model roughness, the optimal smoothing factor of coseismic slip inversion is identified as 0.1. As depicted as Fig. 7, the coseismic slip is mainly cumulated at the depth of 3–50 km, and the average value of coseismic slip is 1.35 m. The maximum coseismic slip is 7.60 m, which is located at latitude of  $-31.13^\circ$ , longitude of  $-72.06^\circ$ , and depth of 14.59 m. The moment released by this earthquake is equivalent to a moment magnitude of  $\sim 8.2$ , the maximum stress drop is 4.34 MPa, and the fitting coefficient of the inversion data and the model reaches 0.9998. The inversion results of the coseismic slip distribution of this earthquake are highly consistent with the results of Heidarzadeh et al. (2016), Okuwaki et al. (2016) and Williamson et al. (2017).

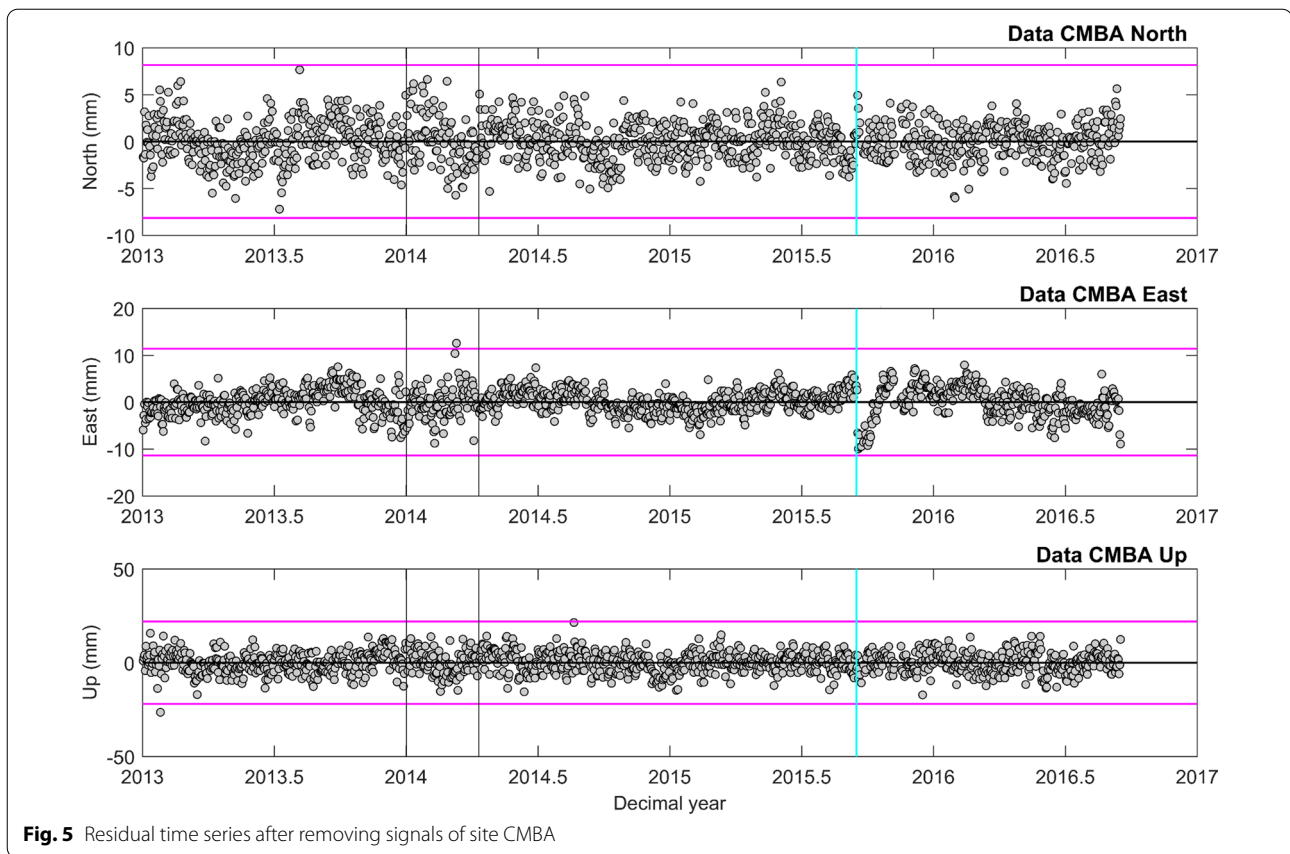


**Fig. 5** Residual time series after removing signals of site CMBA

### Postseismic slip inversion

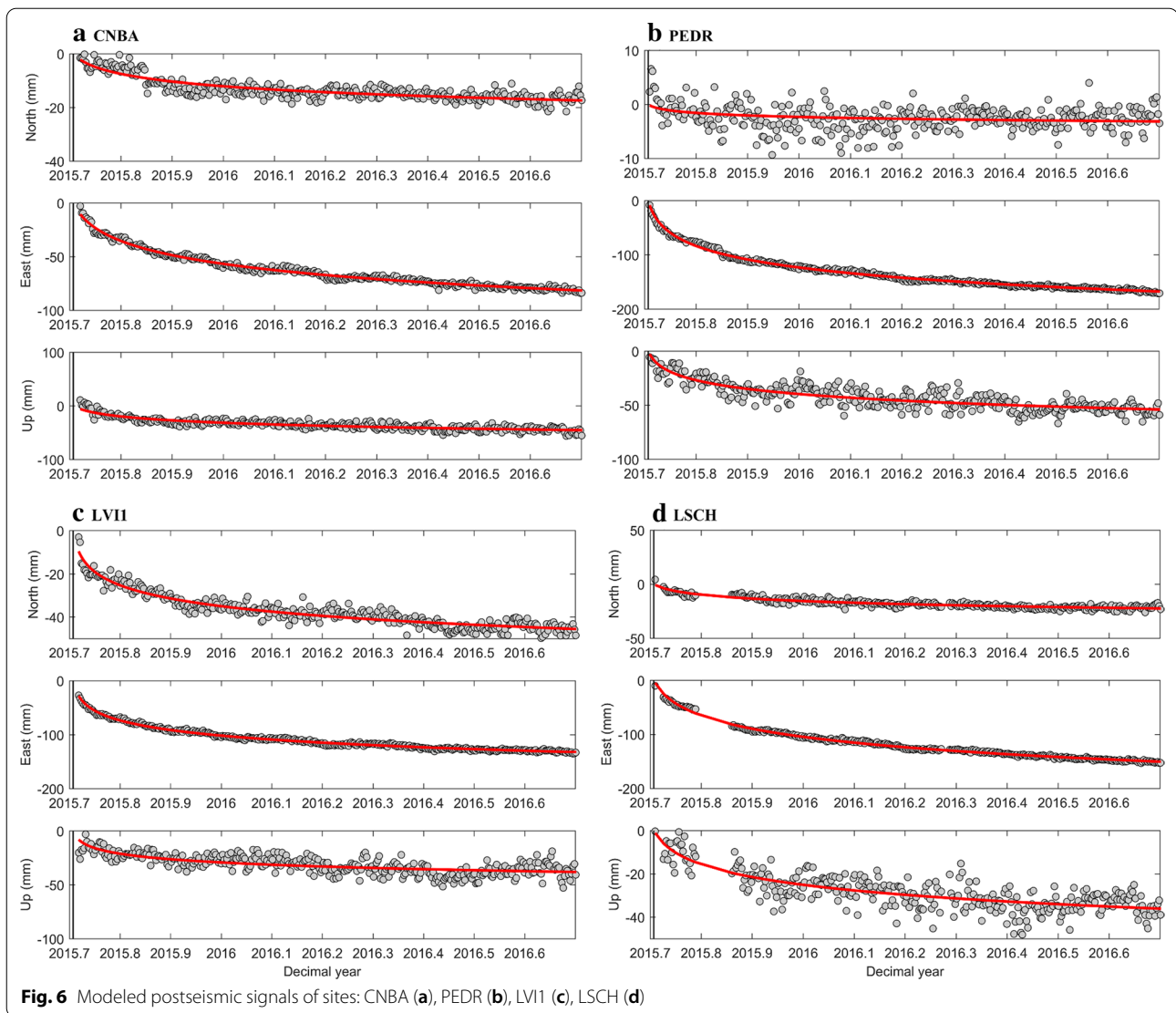
Numerous studies have indicated that the effects of after-slip are cumulated at the near-field region of the source in the early stage after the earthquake occurrence, while the effects of viscoelastic relaxation are cumulated at the middle- and far-field regions in the long-term period (Perfettini and Avouac 2014; Feigl and Thatcher 2006; Hsu et al. 2006; Ozawa et al. 2011; Bedford et al. 2013). Meanwhile, Shrivastava et al. (2016) and Barnhart et al. (2016) also confirmed that the postseismic deformations of the 2015 Illapel earthquake in the near-field region is induced by afterslip, and the effect of viscoelastic relaxation can be neglected.

Thus, we attribute the postseismic deformations in the near-field region of this earthquake to afterslip, and then ignore the effects of the viscoelastic relaxation on the near-field region. The fault model similar to coseismic slip inversion is utilized to characterize the postseismic slip. Considering that afterslip is usually generated around coseismic slip region, the fault model is slightly extended to both sides and deep, thus constructing the length and width of 324 and 170 km along the strike and dip. Similarly, the fault model is divided into  $10 \times 10$  km sub-faults, and the number of sub-faults is 544.

According to the method described in Sect. 2.2, the postseismic signals at 13 GNSS sites are extracted, and the cumulative deformations of 1 year after this earthquake are determined (see Fig. 8). Unlike the coseismic deformation field, large postseismic deformations occur at site PFRJ in the east component, which reaches  $-240.8$  mm. Whereas, the nearest site EMAT do not produce the largest postseismic deformation, suggesting that postseismic slip may present different spatial distribution in comparison with coseismic slip. Meanwhile, the postseismic deformations decay slowly with the increase of epicentral distance, which is different from the coseismic deformation field. The postseismic deformations of 13 sites vary from  $-240.8$  to  $-25.0$  and  $-42.8$  to  $19.7$  mm in the east and north component, while it ranges from  $-60.9$  to  $54.5$  mm in the vertical component. In the vertical direction, most GNSS sites appear a downward trend, and the largest deformation reaches  $-60.9$  mm at site CMBA.

Based on the postseismic deformations and fault model, the postseismic slip can be determined under the layered medium model, and Fig. 8 describes the spatial distribution of afterslip. Similarly, the trade-off value of data misfit and model roughness is regarded as



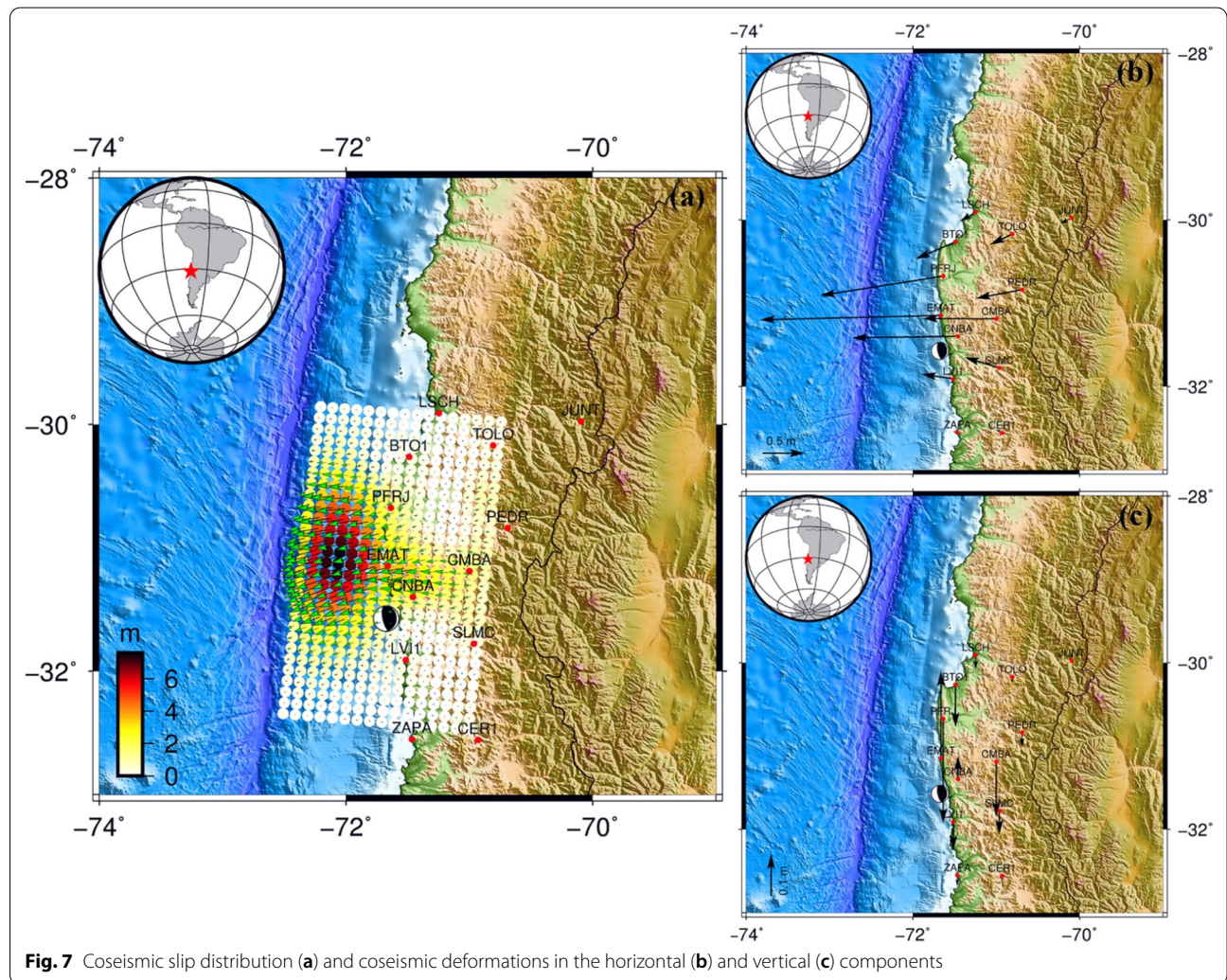


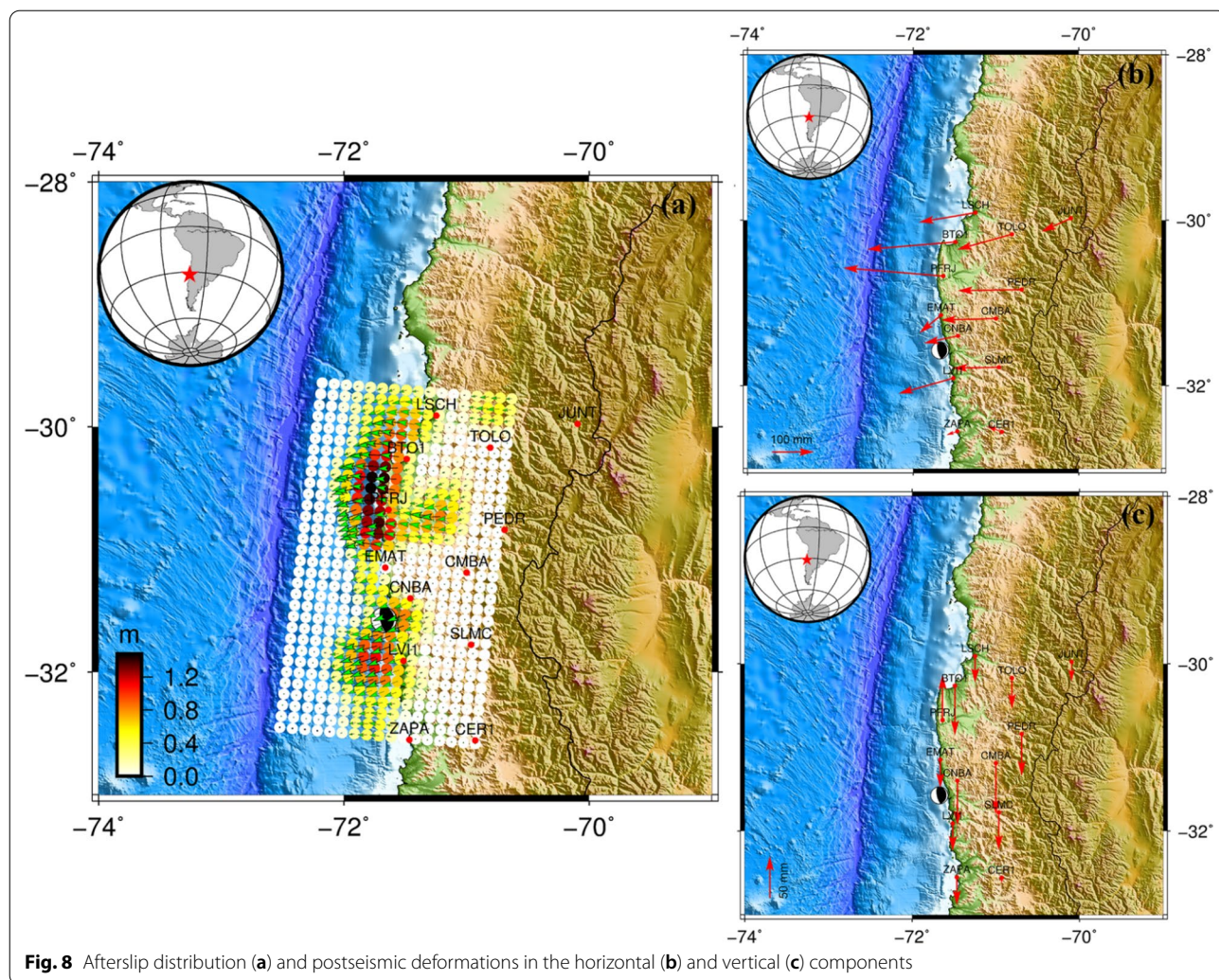
the optimal smoothing factor, and the smoothing factor of postseismic slip inversion is 0.08. Compared with coseismic slip, the afterslip is extended to both deep and two sides, and two peak slip patches are formed on the north and south sides. The afterslip is distributed around the region of coseismic slip and partially overlaps. For the two peak slip areas, the larger slip area is situated at the north side, while the smaller slip area is located near the source. The afterslip is mainly cumulated at the depth of 10–50 km, and the maximum afterslip reaches 1.46 m, which is situated at latitude of  $-30.50^\circ$ , longitude of  $-71.78^\circ$ , and depth of 18.94 m. The released moment of afterslip during the one year after this earthquake is equivalent to a moment magnitude of  $\sim 7.6$ , the maximum stress drop is 1.43 MPa, and the fitting coefficient of the inversion data and the model reaches 0.9929. Shrivastava et al. (2016) utilized

coseismic deformations and the GNSS observations of 43 days after the 2015 Illapel earthquake to explore the coseismic and early afterslip, and confirmed that the afterslip was distributed around the region of coseismic slip, and forming two peak slip areas on both sides. Barnhart et al. (2016) adopted the data sets of InSAR and GNSS to characterize the coseismic and early (i.e., 38 days) postseismic fault slip for the 2015 Illapel earthquake, and demonstrated that two slip areas P1 and P2 are formed after this earthquake. In terms of spatial distribution, the afterslip characterized by GNSS observations of 1 year after this earthquake is consistent with the conclusions of the above studies. Whereas, the region of postseismic slip is slightly enlarged, and the magnitude of fault slip in each patch is increased accordingly.

**Table 1** Coseismic offsets and the accumulated deformations during 1 year after this earthquake of 13 GNSS sites

Site	Coseismic offset (m)			Postseismic deformation (mm)		
	North	East	Up	North	East	Up
BTO1	-0.2066	-0.4802	-0.1014	-17.75	-212.69	-58.98
CER1	0.0396	-0.0695	-0.0132	14.10	-35.42	-6.26
CMBA	0.0038	-0.8792	-0.1316	-3.59	-132.36	-60.96
CNBA	-0.0186	-1.2689	0.0556	-17.37	-81.57	-53.19
EMAT	-0.0526	-2.1681	0.2084	-42.80	-51.81	-33.54
JUNT	-0.0665	-0.1366	0.0179	-32.29	-71.09	-22.92
LSCH	-0.1051	-0.1816	-0.0335	-23.12	-136.13	-31.91
LV11	0.058	-0.3807	-0.068	-37.27	-132.39	-32.66
PEDR	-0.1024	-0.5528	-0.0339	-2.42	-153.72	-49.91
PFRJ	-0.2333	-1.4716	-0.2503	19.67	-240.84	54.50
SLMC	0.1273	-0.4157	-0.0567	-2.03	-112.01	-44.61
TOLO	-0.1265	-0.2657	-0.0141	-36.80	-132.17	-36.49
ZAPA	0.0122	-0.048	-0.0252	-7.99	-25.01	-33.09





**Spatial-temporal evolution of afterslip**

In order to characterize the spatial-temporal evolution of afterslip, the time span of 1 year after this earthquake is divided into 6 time periods (i.e., 0–30, 0–60, 0–120, 0–180, 0–270, and 0–365 days). Meanwhile, the constructed logarithmic or exponential model of postseismic signal is adopted to determine the cumulative postseismic deformation in each time period. According to the postseismic deformation of each time period and the fault model constructed in postseismic slip inversion, the postseismic slip of each time period is inverted under the layered medium model. As depicted in Fig. 9, two slip patches are formed on both sides in the deep, which are the large area on the north side and small area near the source, respectively. After that, the fault slip is continued along the two patches, and the area and magnitude of fault slip is enlarged accordingly. The spatial distribution of fault slip varies significantly in the first 4 time periods, while there is no obvious variation in the last 2

time periods. The result suggests that the fault activity is more obvious during the 180 days after the earthquake, and the fault tends to be stable during the time span of 270–365 days.

Moreover, the postseismic slip during the time period of 0–30 is the largest, and the maximum of fault slip and corresponding slip rate reaches 0.62 m and 20.6 mm/day (see Table 2). Compared with the first time period, the rate of fault slip during the time period of 30–60 is significantly decreased. The maximum of fault slip during the second time period is 0.22 m, and the corresponding slip rate is 7.3 mm/day. For the following 2 time periods (i.e., 60–120 and 120–180 days), the maximum of fault slip is 0.23 and 0.14 m, and the rates of fault slip are continuously decreased, which is 3.8 and 2.3 mm/day, respectively. For the time period of 180–270 and 270–365 days, the maximum of fault slip is 0.14 and 0.11 m, and the corresponding rate of fault slip is 1.6 and 0.9 mm/day, which is relatively small in comparison with other time periods.

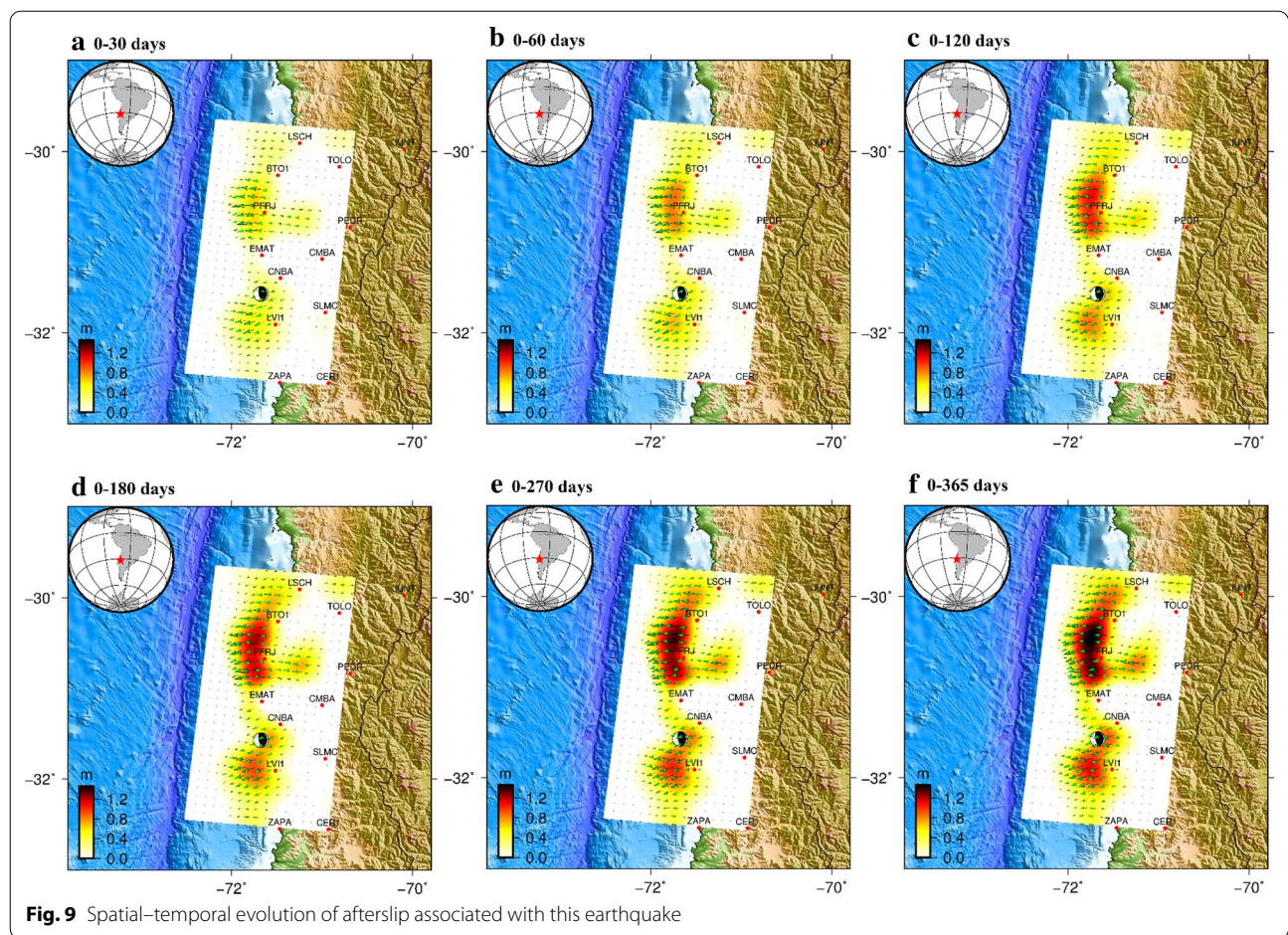


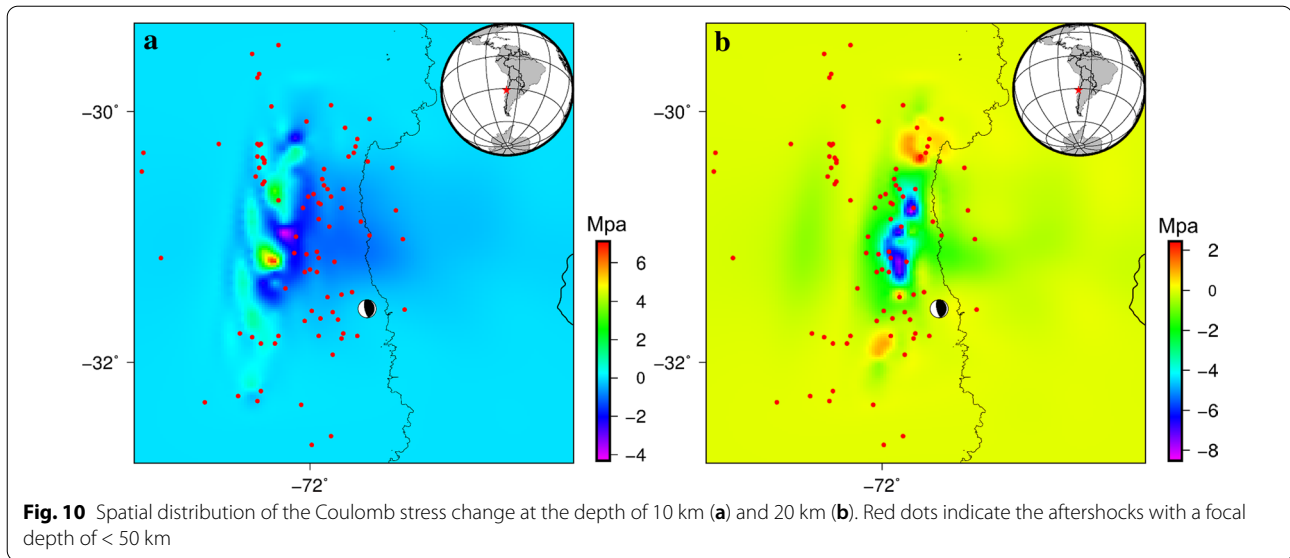
**Table 2** The result of postseismic slip inversion of 6 time periods

Time span (days)	Mean slip (m)	Max stress drop (GPa)	Max slip		Data-model correlation	Mw
			Value (m)	Depth (km)		
0–30	0.09	0.62	0.62	18.94	0.9931	7.38
0–60	0.13	0.82	0.84	18.94	0.9930	7.47
0–120	0.17	1.05	1.07	18.94	0.9929	7.55
0–180	0.19	1.18	1.21	18.94	0.9929	7.59
0–270	0.22	1.32	1.35	18.94	0.9929	7.62
0–365	0.24	1.43	1.46	18.94	0.9929	7.64

The above results indicate that postseismic slip occurs during the 1 year after the earthquake, and it reaches largest during the time period of 0–30 days. Meanwhile, the maximum rate of fault slip during the last 2 time periods is only around 1 mm/day, suggesting that large postseismic slip mainly occurs in the early stage, and the fault tends to be stable as time goes on.

**Coulomb stress change**

Generally, coseismic stress tends to transfer after large earthquake, which may relate to seismic activities around the coseismic rupture area (Steacy 2005; Freed 2005). Thus, investigating the Coulomb stress change induced by coseismic slip helps to understand the triggering mechanism of postseismic fault slip motions and assess the postseismic disaster risk. The Coulomb stress change can be calculated based on the Coulomb failure criterion (King et al. 1994;



Stein 2000; Piombo et al. 2005, 2007; Shan et al. 2013), which is expressed as:

$$\Delta\text{CFS} = \Delta\tau_s - \mu' \Delta\sigma_n,$$

where  $\Delta\text{CFS}$  denotes the Coulomb failure stress (CFS) change,  $\Delta\tau_s$  and  $\Delta\sigma_n$  are the shear and normal stress change on the receiver fault, and  $\mu'$  is the equivalent friction coefficient. In this paper, the PSGRN/PSCMP developed by Wang et al. (2006) is utilized to estimate the static Coulomb stress change, and a moderate effective coefficient (i.e., 0.4) is selected as the equivalent friction coefficient.

Figure 10 presents the spatial distribution of coseismic Coulomb stress change induced by the Illapel earthquake at the depth of 10 and 20 km. The coseismic Coulomb stress change demonstrate that the magnitude of stress increase in the main rupture area induced by the Illapel earthquake reaches several MPa, and the Coulomb stress change present complex characteristics and diversity at different depths. For the depth of 10 km, the magnitude of Coulomb stress change ranges from  $-4$  to  $7$  MPa, and the stress shadow covers most region, suggesting that the stress in this region is mainly released by coseismic rupture. As for the depth of 20 km, the Coulomb stress change shows different spatial distribution in comparison with the depth of 10 km. The Coulomb stress change appears in the region surrounding the coseismic slip and present a good correlation with the aftershocks and afterslip activities. The Coulomb stress increase also forms two peak areas on both the north and south sides, and the

magnitude reaches about 2 MPa. The Coulomb stress change between the two peak areas is negative, and most aftershocks also gather in this area, implying that the coseismic Coulomb stress in this area is uploaded by these aftershocks. Meanwhile, the result of Sect. 3.3 indicates that the postseismic slip is mainly cumulated at the depth of 10–50 km, and the maximum slip is situated at the depth of 18.94 m. The spatial distribution of afterslip suggests that the afterslip is extended to both deep and two sides, and two peak slip patches are formed on the north and south sides. Thus, on basis of the above analysis, we conclude that the postseismic slip after the Illapel earthquake may be triggered by the stress increase in the deep region induced by coseismic phase.

## Conclusion

In this study, the daily GNSS position time series of 13 sites with time span of 1 year after the earthquake is utilized to characterize the postseismic deformation mechanism and spatial–temporal properties of postseismic slip. Firstly, we design a scheme to extract the postseismic signal from GNSS position time series, which can extract and model the postseismic signal with consideration of the background tectonic movement and the influence of noise. Then, the coseismic slip is determined based on the coseismic deformations and fault model, which can be regarded as a reference to understand the postseismic deformation effects. At last, according to the postseismic signals and fault model, the spatial–temporal properties of afterslip is explored. The main conclusions are listed as follows:

- (1) The postseismic signal extraction and modeling method introduced in this paper can effectively extract the postseismic signal and establish simulation function model with consideration of the influence of background tectonic movement. Meanwhile, the parameters of GNSS position time series are estimated by means of holistic modeling, which can effectively reduce errors introduced by segmented processing.
- (2) Comparing with coseismic slip, the afterslip is extended to both deep and two sides, and two peak slip patches are formed on the north and south sides. For the two peak slip areas, the larger slip area is situated at the north side, while the smaller slip area is located near the source. The afterslip is mainly cumulated at the depth of 10–50 km, and the maximum of postseismic slip reaches 1.46 m, which is situated at latitude of  $-30.50^\circ$ , longitude of  $-71.78^\circ$ , and depth of 18.94 m.
- (3) The postseismic fault slip occurs during the 1 year after the earthquake, and it reaches largest during the time period of 0–30 days. The maximum rate of fault slip during the last 2 time period is only around 1 mm/day, suggesting that large postseismic slip mainly occurs in the early stage, and the fault tend to be stable as time goes on. Meanwhile, the Coulomb stress change denote that the stress increase in the deep region induced by coseismic phase contribute to the occurrence of afterslip associated with this earthquake.

#### Acknowledgements

We are very grateful to Nevada Geodetic Laboratory (NGL) for providing GNSS position time series.

#### Author's contributions

JY led the research work. JY and YX designed the study and proposed crucial suggestions for the manuscript. YX and ZJ processed the data and performed the experiments. YX wrote the first draft of the manuscript. All authors read and approved the final manuscript.

#### Funding

This study is support by the Fundamental Research Funds for the Central Universities (2019B60614), Postgraduate Research and Practice Innovation Program of Jiangsu Province (SJKY19\_0514), and National Key R&D Program of China (No. 2018YFC1508603).

#### Availability of data and materials

The GNSS position time series used in this paper are provided by Nevada Geodetic Laboratory (NGL), which are available at <http://geodesy.unr.edu/>.

#### Competing interests

The authors declare that they have no competing interests.

#### Author details

<sup>1</sup> College of Civil Engineering, Nanjing Forestry University, Nanjing 210037, China. <sup>2</sup> School of Earth Sciences and Engineering, Hohai University, Nanjing 211100, China. <sup>3</sup> Faculty of Geosciences and Environmental Engineering, Southwest Jiaotong University, Chengdu 611756, China.

Received: 16 October 2020 Accepted: 20 January 2021  
Published online: 26 January 2021

#### References

- Barnhart WD, Murray JR, Briggs RW, Gomez F, Miles CPJ et al (2016) Coseismic slip and early afterslip of the 2015 Illapel, Chile, earthquake: implications for frictional heterogeneity and coastal uplift. *J Geophys Res Solid Earth* 121:6172–6191
- Bedford J, Moreno M, Baez JC, Lange D, Tilmann F, Rosenau M et al (2013) A high-resolution, time-variable afterslip model for the 2010 Maule Mw = 8.8, Chile megathrust earthquake. *Earth Planet Sci Lett* 383:26–36
- Bruhat L, Barbot S, Avouac JP (2011) Evidence for postseismic deformation of the lower crust following the 2004 Mw 6.0 Parkfield earthquake. *J Geophys Res Solid Earth* 116:B08401
- Chen KJ, Ge MR, Babeyko A, Li XX, Diao FQ, Tu R (2016) Retrieving real-time co-seismic displacements using GPS/GLONASS: a preliminary report from the September 2015 Mw 8.3 Illapel earthquake in Chile. *Geophys J Int* 206:941–953
- Diao F, Xiong X, Wang R (2011) Mechanism of transient post-seismic deformation following the 2001 Mw 7.8 Kunlun (China) earthquake. *Pure Appl Geophys* 168:767–779
- Diao F, Xiong X, Zheng Y (2012) Static slip model of the Mw 9.0 Tohoku (Japan) earthquake: results from joint inversion of terrestrial GPS data and sea-floor GPS/acoustic data. *China Sci Bull* 57(16):1990–1997
- Diao F, Wang R, Wang Y, Xiong X, Walter TR (2018) Fault behavior and lower crustal rheology inferred from the first seven years of postseismic GPS data after the 2008 Wenchuan earthquake. *Earth Planet Sci Lett* 495:202–212
- Ding KH, Freymueller TJ, Wang Q, Zou R (2015) Coseismic and early post-seismic deformation of the 5 January 2013 mw 7.5 Craig earthquake from static and kinematic GPS solutions. *Bull Seismol Soc Am* 105(2):1153–1164
- Feigl KL, Thatcher W (2006) Geodetic observations of post-seismic transients in the context of the earthquake deformation cycle. *CR Geosci* 338:1012–1028
- Freed AM (2005) Earthquake triggering by static, dynamic, and postseismic stress transfer. *Annu Rev Earth Planet Sci* 33:335–367
- Freed AM (2007) Afterslip (and only afterslip) following the 2004 Parkfield California earthquake. *Geophys Res Lett* 34(6):L06312
- Guo JY, Yuan YD, Kong QL, Li GW, Wang FJ (2012) Deformation caused by the 2011 eastern japan great earthquake monitored using the GPS single-epoch precise point positioning technique. *Appl Geophys* 9(4):483–493
- Heidarzadeh M, Murotani S, Satake K, Ishibe T, Gusman AR (2016) Source model of the 16 September 2015 Illapel, Chile, Mw 8.4 earthquake based on teleseismic and tsunami data. *Geophys Res Lett* 43:643–650
- Hoechner A, Sobolev SV, Einarsson I, Wang R (2012) Investigation on afterslip and steady state and transient rheology based on postseismic deformation and geoid change caused by the Sumatra 2004 earthquake. *Geochem Geophys Geosyst* 12:Q07010
- Hreinsdottir S, Freymueller TJ, Bürgmann R, Mitchell J (2006) Coseismic deformation of the 2002 Denali fault earthquake: insights from GPS measurements. *J Geophys Res Solid Earth* 111:B03308
- Hsu YJ, Bechor N, Segall P et al (2002) Rapid afterslip following the 1999 Chi-Chi, Taiwan earthquake. *Geophys Res Lett* 29(16):1754
- Hsu YJ, Simons M, Avouac JP et al (2006) Frictional afterslip following the 2005 Nias-Simeulue earthquake, Sumatra. *Science* 312:1921–1926
- Huang H, Meng LS, Bürgmann R et al (2017) Early aftershocks and afterslip surrounding the 2015 Mw 8.4 Illapel rupture. *Earth Planet Sci Lett* 457:282–291
- Jiang Z, Yuan L, Huang D, Yang Z, Chen W (2017) Postseismic deformation associated with the 2008 Mw 7.9 Wenchuan earthquake, China: constraining fault geometry and investigating a detailed spatial distribution of afterslip. *J Geodyn* 112:12–21
- Jiang ZS, Yuan LG, Huang DF, Yang ZR, Hassan A (2018) Postseismic deformation associated with the 2015 Mw 7.8 Gorkha earthquake, Nepal: investigating ongoing afterslip and constraining crustal rheology. *J Asian Earth Sci* 156:1–10
- King GCP, Stein RS, Lin J (1994) Static stress change and the triggering of earthquakes. *Bull Seismol Soc Am* 84:935–953

- Kreemer C, Blewitt G, Maerten F (2006) Co- and post-seismic deformation of the 28 March 2005 Nias Mw 8.7 earthquake from continuous GPS data. *Geophys Res Lett* 33:L07307
- Melgar D, Fan W, Riquelme S, Geng J, Liang C, Fuentes M et al (2016) Slip segmentation and slow rupture to the trench during the 2015, Mw 8.3 Illapel, Chile earthquake. *Geophys Res Lett* 43:961–966
- Okuwaki R, Yagi Y, Aránguiz R, González J, González G (2016) Rupture process during the 2015 Illapel, Chile earthquake: zigzag-along-dip rupture episodes. *Pure Appl Geophys* 173(4):1011–1020
- Ozawa S, Nishimura T, Suito H, Kobayashi T, Tobita M, Imakiire T (2011) Coseismic and postseismic slip of the 2011 magnitude-9 Tohoku-Oki earthquake. *Nature* 475(7356):373–376
- Ozawa S, Nishimura T, Munekane H, Suito H, Kobayashi T, Tobita M, Imakiire T (2012) Preceding, coseismic, and postseismic slips of the 2011 Tohoku earthquake, Japan. *J Geophys Res Solid Earth* 117:B07404
- Perfettini H, Avouac JP (2014) The seismic cycle in the area of the 2011 Mw 9.0 Tohoku-Oki earthquake. *J Geophys Res Solid Earth* 119:4469–4515
- Piombo A, Martinelli G, Dragoni M (2005) Post-seismic fluid flow and Coulomb stress change in a poroelastic medium. *Geophys J Int* 162:507–515
- Piombo A, Tallarico A, Dragoni M (2007) Displacement, strain and stress fields due to shear and tensile dislocations in a viscoelastic half-space. *Geophys J Roy Astron Soc* 170(3):1399–1417
- Pollitz FF, Burgmann R, Banerjee P (2006) Post-seismic relaxation following the great 2004 Sumatra-Andaman earthquake on a compressible self-gravitating Earth. *Geophys J Int* 167:397–420
- Ruiz S, Klein E, Campo FD, Rivera E, Fleitout L (2016) The seismic sequence of the 16 September 2015 Mw 8.3 Illapel, Chile, earthquake. *Seismolog Res Lett* 87(4):789–799
- Segall P, Davis JL (1997) GPS applications for geodynamics and earthquake studies. *Ann Rev Earth Planet Sci* 25:301–336
- Shan B, Xiong X, Wang R, Zheng Y, Yang S (2013) Coulomb stress evolution along Xianshuihe-Xiaojiang Fault System since 1713 and its interaction with Wenchuan earthquake, May 12, 2008. *Earth Planet Sci Lett* 377–378:199–210
- Shen ZK et al (2009) Slip maxima at fault junctions and rupturing of barriers during the 2008 Wenchuan earthquake. *Nat Geosci* 2(10):718–724
- Shen ZK, Wang M, Zeng Y, Wang F (2015) Optimal interpolation of spatially discretized geodetic data. *Bull Seismol Soc Am* 105:2117–2127
- Shrivastava MN, González G, Moreno M, Chlieh M, Salazar P, Reddy CD et al (2016) Coseismic slip and afterslip of the 2015 Mw 8.3 Illapel (Chile) earthquake determined from continuous GPS data. *Geophys Res Lett* 43:10710–10719
- Simons M et al (2011) The 2011 magnitude 9.0 Tohoku-Oki Earthquake: mosaicking the megathrust from seconds to centuries. *Science* 332:1421–1425
- Steady S (2005) Introduction to special section: stress transfer, earthquake triggering, and time-dependent seismic hazard. *J Geophys Res Solid Earth* 110:B05501
- Stein RS (2000) The role of stress transfer in earthquake occurrence. *Transl World Seismol* 402:605–609
- Tobita M (2016) Combined logarithmic and exponential function model for fitting postseismic GNSS time series after 2011 Tohoku-Oki earthquake. *Earth Planet Space* 68(1):41. <https://doi.org/10.1186/s40623-016-0422-4>
- Wang R, Martin FL, Roth F (2003) Computation of deformation induced by earthquakes in a multi-layered elastic crust—FORTRAN programs EDGRN/EDCMP. *Comput Geosci* 29(2):195–207
- Wang R, Lorenzo-Martín F, Roth F (2006) PSGRN/PSCMP—a new code for calculating co- and post-seismic deformation, geoid and gravity change based on the viscoelastic-gravitational dislocation theory. *Comput Geosci* 32:527–541
- Wang R, Diao F, Hoehner A (2013) SDM—a geodetic inversion code incorporating with layered crust structure and curved fault geometry. In: *Proceedings of the EGU General Assembly 2013 Vol. 15, EGU2013-2411-1*
- Williamson A, Newman A, Cummins P (2017) Reconstruction of coseismic slip from the 2015 Illapel earthquake using combined geodetic and tsunami waveform data. *J Geophys Res Solid Earth* 122:2119–2130
- Zhou M, Guo J, Liu X, Shen Y, Zhao C (2020) Crustal movement derived by GNSS technique considering common mode error with MSSA. *Adv Space Res* 66(8):1819–1828

### Publisher's Note

Springer Nature remains neutral with regard to jurisdictional claims in published maps and institutional affiliations.

Submit your manuscript to a SpringerOpen® journal and benefit from:

- Convenient online submission
- Rigorous peer review
- Open access: articles freely available online
- High visibility within the field
- Retaining the copyright to your article

Submit your next manuscript at ► [springeropen.com](https://www.springeropen.com)